Provided for non-commercial research and education use.
Not for reproduction, distribution or commercial use.

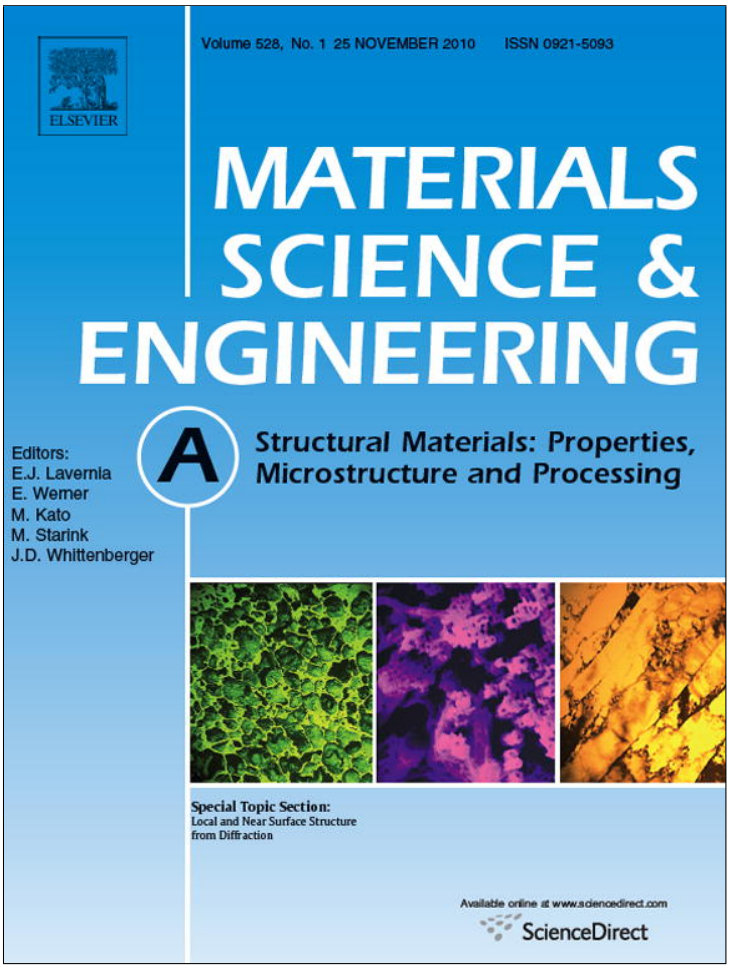

This article appeared in a journal published by Elsevier. The attached copy is furnished to the author for internal non-commercial research and education use, including for instruction at the authors institution and sharing with colleagues.

Other uses, including reproduction and distribution, or selling or licensing copies, or posting to personal, institutional or third party websites are prohibited.

In most cases authors are permitted to post their version of the article (e.g. in Word or Tex form) to their personal website or institutional repository. Authors requiring further information regarding Elsevier's archiving and manuscript policies are encouraged to visit:

http://www.elsevier.com/copyright

Author's personal copy

Materials Science and Engineering A 528 (2010) 11–27

Contents lists available at ScienceDirect

Materials Science and Engineering A

journal homepage: www.elsevier.com/locate/msea

Thermo-mechanical processing in a synchrotron beam☆

Klaus-Dieter Liss[a,*], Kun Yan[a,b]

[a] Australian Nuclear Science and Technology Organisation, The Bragg Institute, New Illawarra Road, Lucas Heights, NSW 2234, Australia
[b] Faculty of Engineering, University of Wollongong, Wollongong, NSW 2522, Australia

ARTICLE INFO

Article history:
Received 15 March 2010
Received in revised form 4 June 2010
Accepted 8 June 2010

Keywords:
Synchrotron X-ray diffraction
Bulk deformation
Thermo-mechanical processing
Crystal plasticity
Orientation relationships
Recrystallization
Phase transformation

ABSTRACT

Well collimated, high energy X-rays of 90 keV from synchrotron sources have been used to study metals undergoing plastic deformation in situ, in real time and in the bulk of the materials. The spottiness of the Debye–Scherrer rings, showing reflections from individual crystallites, is analyzed to obtain grain statistics, mosaic spread and grain orientation. Upon cold deformation, coarse grained materials show fingerprints of subgrain formation, grain rotation, grain refinement and the evolution from a single grain into the asymptotic texture. Lattice strain, its partition and anisotropy can be simultaneously revealed. Heating of metals under continuous load drives the observation through the regimes of phase transformation and grain relationships therein, grain coarsening, dynamic recovery and dynamic recrystallization. Examples on copper, magnesium, twinning induced plasticity steel, zirconium alloy and titanium aluminium intermetallics are shown.

Crown Copyright © 2010 Published by Elsevier B.V. All rights reserved.

1. Introduction

The mechanical properties of a metallic product depend strongly on both phase composition and microstructure of the polycrystalline material. For example, copper work-hardens under deformation while it becomes soft under thermal treatment, related to grain and subgrain refinement and coarsening, respectively. These effects play a crucial role in applications such as airplane turbine blades or weldings in nuclear reactor vessels. Preferred crystallographic orientation, texture, influences the isotropic behavior of a material and may reflect in enormous cost and waste savings, as in the drink can production by mastering the deep-drawing process or improve the electric current density in high temperature superconductors. Therefore, most development efforts for the design of materials with novel or improved physical properties, like physical strength, ductility, formability deal with the control of the microstructure. Besides the basic physical parameters, the art lies in finding the right thermo-mechanical processing, which for highly designed materials, can be very sophisticated. After production, the lifetime of a metallic product depends on thermo-mechanic load, inducing non-desired effects, such as creep, which may alter the microstructure and thus the mechanical properties. Therefore, physical thermo-mechanic simulation is widely used in industry and research laboratories.

Conventionally, a metal is processed under realistic or model conditions at high temperature, with a defined time and stress profile and then quenched to freeze the structural state from that particular point in parameter space. To access its bulk properties, this specimen is then cut, polished and examined by microscopy or conventional X-ray diffraction in a surface-near region. In order to obtain the materials behavior along all time steps of the thermo-mechanical process, a second, third and many further specimens are prepared from slightly different temperature or stress states and subsequently analyzed in the same way. Obviously, this method is extremely time consuming and it is most doubtful, that the microstructure during the processing is still the same after quenching, particularly when inevitable phase transformations are involved.

Modern neutron and synchrotron X-ray sources are bright enough to study thermo-mechanical processes in situ, in real time, and from the bulk of the material. This elucidates the material behavior during heat treatment, or after heat treatment during cooling, and allows to define the best process temperatures for a specific material. Particular advantages of the neutron diffraction method are the extraordinary penetration, a good average over large volumes in grain statistics, and different atomic contrasts allowing to study order–disorder transitions.

Like neutrons, high energy X-rays from synchrotrons such as configured at the European Synchrotron Radiation Facility (ESRF) in France or the Advanced Photon Source (APS) in the USA show competitive deep penetration of centimeters into the bulk of the material [1]. In contrast, the synchrotron beam is sharply bundled and may reflect only from a small number of grains. With the

☆ Probing Strains and Dislocation Gradients with Diffraction.

* Corresponding author. Tel.: +61 2 9717 9479; fax: +61 2 9717 3606.
E-mail addresses: liss@kdliss.de, kdl@ansto.gov.au (K.-D. Liss).

0921-5093/$ – see front matter. Crown Copyright © 2010 Published by Elsevier B.V. All rights reserved.
doi:10.1016/j.msea.2010.06.017

Author's personal copy

only recently available, time resolving large area detectors, high quality X-ray movies can be taken while the specimen undergoes thermo-mechanic simulation. Minute understanding of the X-ray diffraction process, the underlying crystallography and software development allow to extract novel and multi-dimensional information from the recorded patterns [2–5].

2. Experimental

The third generation synchrotrons APS and ESRF have been used for the present studies. The high electron-energy rings of 7 GeV and 6 GeV provide undulator radiation in the high energy X-ray regime into the beamlines 1-ID and ID15B, respectively. Silicon monochromators are used to define the incident beam at about energy $E = 90$ keV with wavenumber $k = 45.6$ Å^{-1} and wavelength $\lambda = 2\pi/k = 0.138$ Å feeding an experimental hutch containing a typical setup as given in Fig. 1. The Ø ∼ 100 μm beam impinges onto the polycrystalline sample of typical 4 mm thickness in transmission mode and is diffracted into Debye–Scherrer cones, which are recorded in about 1.0–1.5 m distance by a flat panel detector, oriented strictly perpendicular to the incident beam. The small diffraction angles of high energy X-rays allow to record simultaneously full diffraction rings up to typically 10 Å^{-1}. At APS we used the amorphous silicon pixel detector of General Electrics. It consists of 2048 × 2048 pixels of 200 μm × 200 μm size and the electronic hardware was set up to record continuously up to 300 images, here up to 5 Hz frame rate. The ESRF detector was a Pixium 4700 flat panel amorphous silicon detector [6] with 1920 (h) × 2640 (v) pixels measuring 154 μm × 154 μm, continuously streaming with 2.5 Hz including a dead time of a few 100 ms.

Instrument calibration occurs through a known standard material. The sample to detector distance is obtained by two exposures with known translation of the sample towards the detector measuring the change of size of the diffraction rings and evaluation through the rule of proportion. Then, the accurate beam energy can be calibrated by evaluation of the powder pattern of the standard.

Different sample environments can be set up according to availability and needs.

At APS, we used a stand-alone hydraulic load frame based on a MTS 858 with ±15 kN maximal force. Optionally, an infrared furnace was installed for external heating of the specimen up to 1100 °C. ESRF supplies a compact, hydraulic 5 kN frame with large rotational access of 170° and operation at room temperature or alternatively, a screw driven Instron electro-thermomechanical tester (ETMT) for simulating thermo-mechanical processing. In the present configuration loads up to 3000 N can be applied while the specimen is heated resistively with a maximum power angle of 8 V and 450 A. We have reached melting temperatures of iron and titanium aluminium intermetallics which lie around 1500 °C. Cylindrical and flat sheet bone shaped specimens have been prepared by wire cutting for usage in compression and tensile testing, respectively. Typically, a test starts by mounting the sample into the load frame followed by translational transmission scans to locate the sample center in the beam. Different temperature and stress profiles can be run in both constant load and constant displacement mode. Both facilities allow to record the thermo-mechanical load parameters in their beamline control software based on SPEC [7]. A regulation script was implemented into the control software to

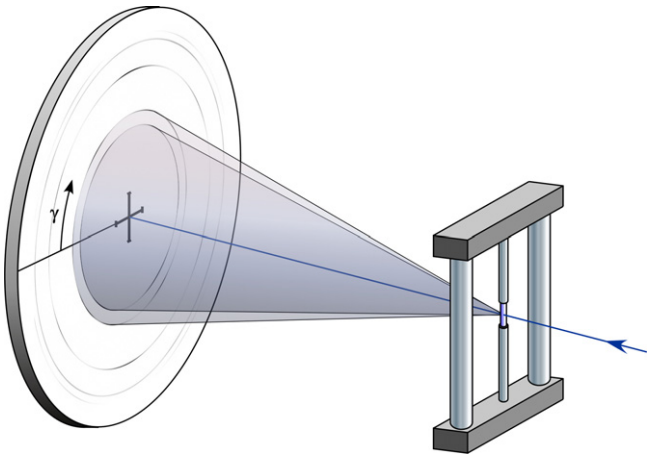

Fig. 1. Experimental setup. A fine synchrotron beam impinges from the right to the polycrystalline specimen and diffracts into Debye–Scherrer cones recorded on a 2D detector.

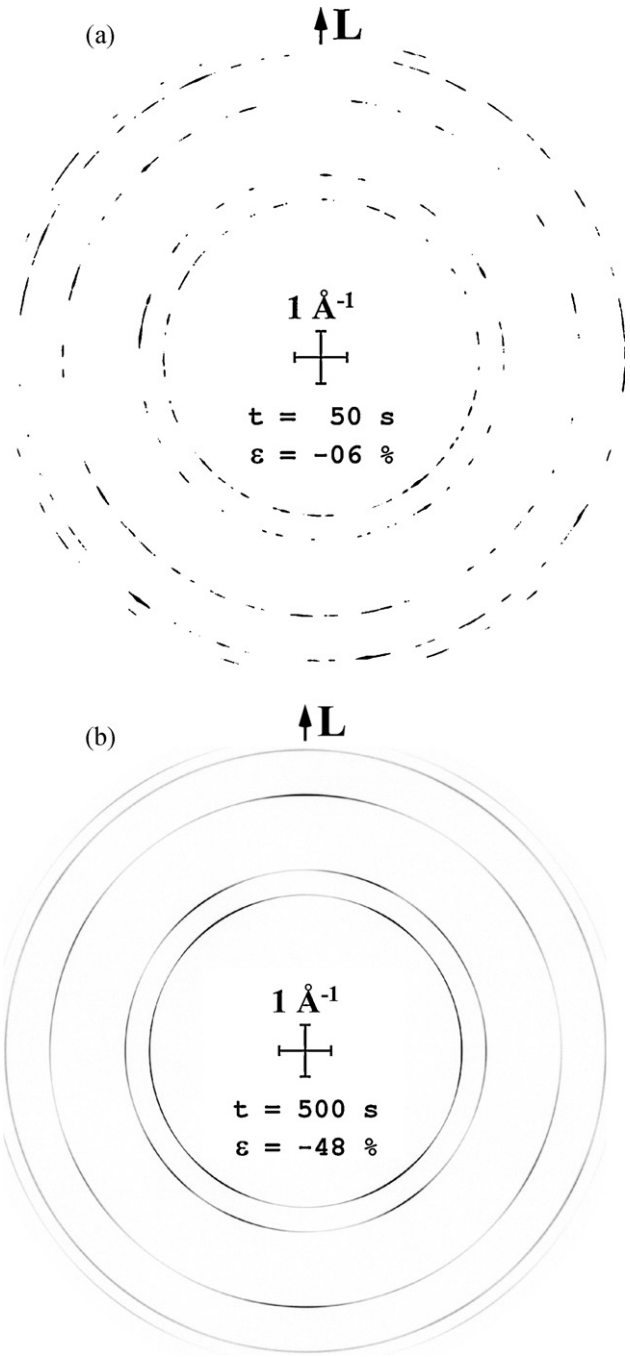

Fig. 2. Two-dimensional diffraction rings from polycrystalline copper recorded towards the beginning (a) and the end (b) of the deformation process.

Author's personal copy

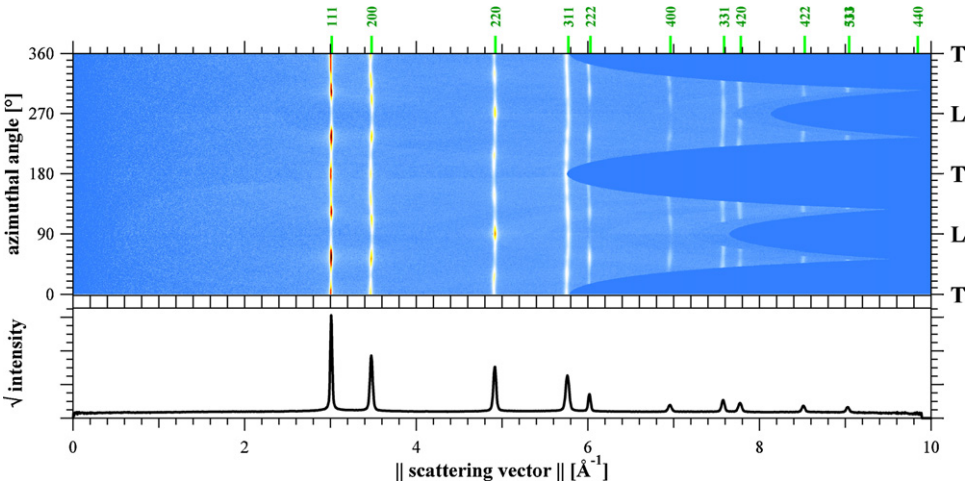

Fig. 3. Intensity from the rings in Fig. 2b straightened into azimuthal-angle/scattering vector plot (top) and integrated diffraction pattern (bottom). The dark shaded region above 5.8 Å^{-1} is missing coverage due to the rectangular detector geometry.

coincide the center of the specimen with the X-ray beam in a continuous loop or before any single exposure frame was taken, ensuring minimal grain motion with respect to the beam.

3. Data evaluation

Diffraction rings from coarse and fine grained copper are shown in Fig. 2. For visualization, they are linearly calibrated to reciprocal space units Q [Å^{-1}], so that they can be directly compared to any powder or single crystal pattern. A computer scripting platform is essential to batch process and extract quantitative information from thousands of images in a row. Therefore, the software package dataRring based on the SCILAB platform and interfaced to the *C* programming language has been written to fit automatically the center of a continuous ring pattern (Fig. 2b), which then can be used for the whole set of corresponding images (Fig. 2a). For each image pixel, the modulus of the scattering vector, or the momentum transfer, $Q = 2\,k\sin(\theta)$ is calculated with Bragg angle θ obtained from $\tan(2\theta) = R/D$, pixel radius R from the center and detector distance D. Azimuthally, the rings can be divided into N sectors of angular step size $\psi_s = 360°/N$ allowing to re-bin the intensities into azimuthal-angle ψ-Q space as depicted in Fig. 3. For each ψ value, the matrix holds a conventional powder diffraction pattern. The orientation of the scattering vector is given by ψ in-plane, inclined by θ out-of-plane and allows for evaluating texture information of the sample. Note, however, that one Debye–Scherrer ring represents only one ring on the pole figure as sketched in Fig. 4, which is by θ smaller than a great circle. A true two-dimensional texture information can be obtained by rotating the sample around the vertical axis sweeping the ring correspondingly on the pole figure. The axis poles, however, are not capped in this way, but since Bragg angles are small, almost full coverage is given and, together with pole figures of the different reflections, sufficient information for an orientation distribution function is supplied.

The information from the ψ-Q space can be evaluated with regards to different aspects. Optionally, a numerical range in Q around a considered refection is chosen, over which the intensity is integrated by summation and interpolated background subtracted. This summation method delivers best intensity values for isolated peaks as it does not depend on a peak shape or lack of statistics at small intensities. Alternatively, a Gaussian, Lorentzian or pseudo-Voight function can be fitted in the designated Q range, refining background, position, amplitude, width and area of the reflection. The latter corresponds to the integrated intensity and should be similar to the summation method. The evaluation of the position is more delicate and can have two different contributions, namely from strain and the geometrical position of the scattering volume in the sample. For continuous rings, Fig. 2b, many grains contribute and the scattering center is just the center of the illuminated sample volume, so that strain $\varepsilon = -\Delta Q/Q$ can be directly evaluated. To avoid systematic errors from the inaccuracy of the ring center, it is advised to average $\Delta Q = (\Delta Q(\psi) + \Delta Q(\psi + 180°))/2$ in the two opposite directions, which is equal to the evaluation of the ring diameters rather than the ring radii. In coarse grained materials, Fig. 2a, diffraction spots appear from individual crystallites, which are not necessarily centered in the illuminated sample volume. On lateral shift, the ring center position for this spot varies correspondingly. If mosaic is large and the opposite reflection is found, evaluation of the ring diameter gives a more accurate strain value while the difference $(\Delta Q(\psi) - \Delta Q(\psi + 180°))$ in peak position is a measure for the lateral displacement of the grain from

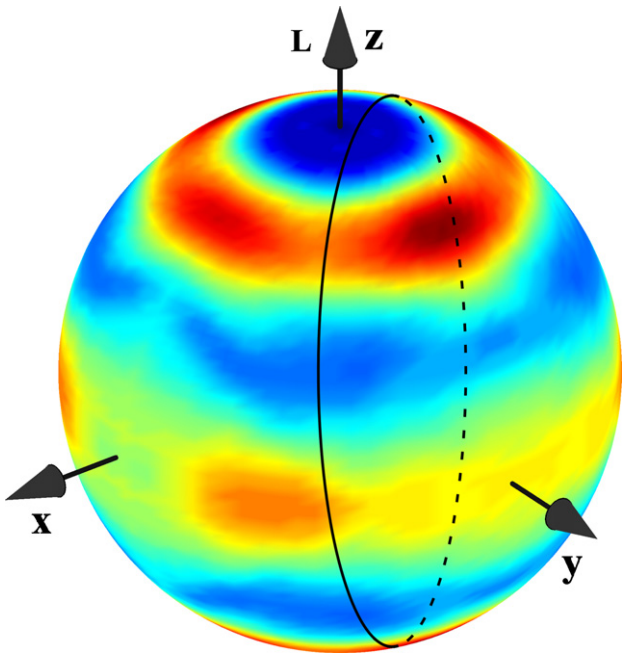

Fig. 4. Full 1 1 1 pole figure of the deformed polycrystalline copper specimen. The ring indicates the orientations corresponding to one 1 1 1 Debye–Scherrer ring (low: blue; high: red) (For interpretation of the references to colour in this figure legend, the reader is referred to the web version of the article.).

Author's personal copy

the beam center. If a grain is misplaced from the scattering center along the beam direction, its effective distance to the detector changes leading to a variation in the appearing Q and care must be taken to separate this systematic effect from lattice strain. One remedy is to change the detector distance and follow the relative change of the radius. If this is not possible due to time restrictions in an in situ experiment, generally larger detector distance D leads to smaller geometric error in Q [8]. Therefore, a large far-field detector placed in distance is better than a high resolution detector positioned too close to the sample. A combination of both has been developed in the three-dimensional X-ray diffraction method [9], with the drawback, it is very time consuming and slow due to multiple exposures.

4. Experimental data, interpretation and results

A series of different sample systems, temperature and load conditions has been studied for both validation of the technique and gaining novel findings in the materials. The intensity distribution and its time evolution on the Debye–Scherrer rings holds information about grain size, grain imperfection, grain orientation, grain correlations, grain rotation, grain refinement, grain

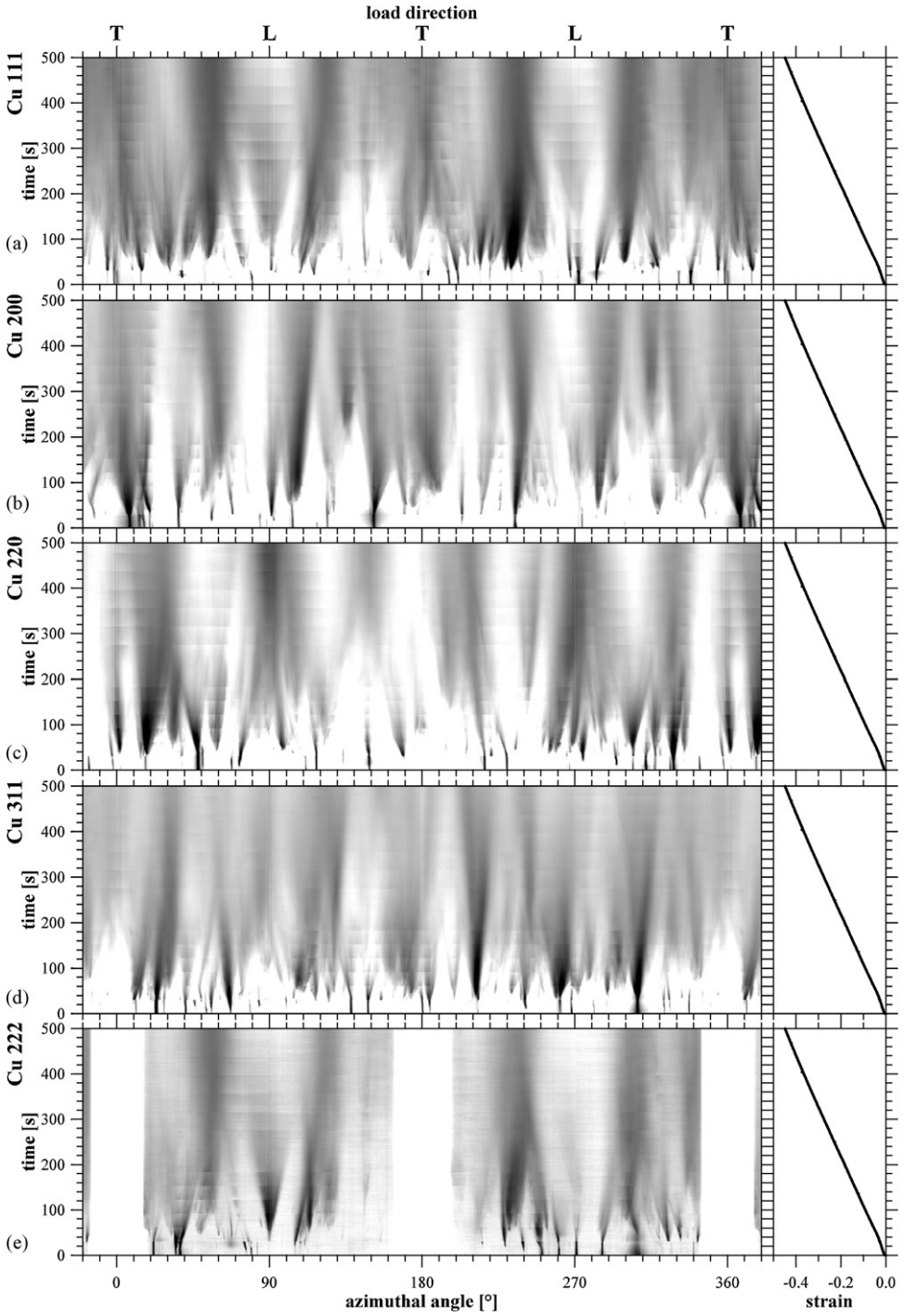

Fig. 5. Azimuthal-angle/time plots for compression of polycrystalline copper.

Author's personal copy

coarsening and grain displacement. Some experience has to be established and validated to distinguish between the different physical processes leading to structural changes, such as crystallographic and dislocation slip, twinning, subgrain formation, recovery, grain growth, recrystallization. These aspects will be emphasized on different examples, leading to the ability of reading the azimuthal-angle/time plots as one reads a microscopy image routinely. The information in each of both, however, is not a complete answer to the system, but leads to very complementary and valuable information.

4.1. Cold deformation of copper

Cylindrical, coarse grained copper samples of Ø 3 mm and 4.5 mm height with a grain size of ~300 μm were prepared from electric wire material previously annealed for 7200 s at 1173 K and mounted into the 5 kN compression frame of the ESRF setup. Diffraction patterns were taken every 0.5 s, while undergoing continuous compression from 4.5 mm to 2.4 mm in 500 s. Two of them are reproduced in Fig. 2 obtained after 50 s ($\varepsilon = -0.06$) and at the end ($\varepsilon = -0.48$) showing the evolution from a spotty pattern with well separated reflections stemming from single crystallites to continuous rings modulated by the texture of the material. The initial patterns ($\varepsilon = -0.00$) are even sharper and therefore difficult to reproduce for this presentation. Azimuthal-angle/time plots were obtained by cutting the ring patterns at the 9 o'clock position and reproducing the azimuthal intensity distribution on a selected ring into one line at each step in time. Fig. 5 shows the so obtained plots for the first 5 reflections. At time $t = 0$, only very few spots are diffracted, stemming from the limited number of crystallites in the illuminated volume. Since the sample was annealed, crystallites are perfect and the reflections correspondingly sharp. It can be

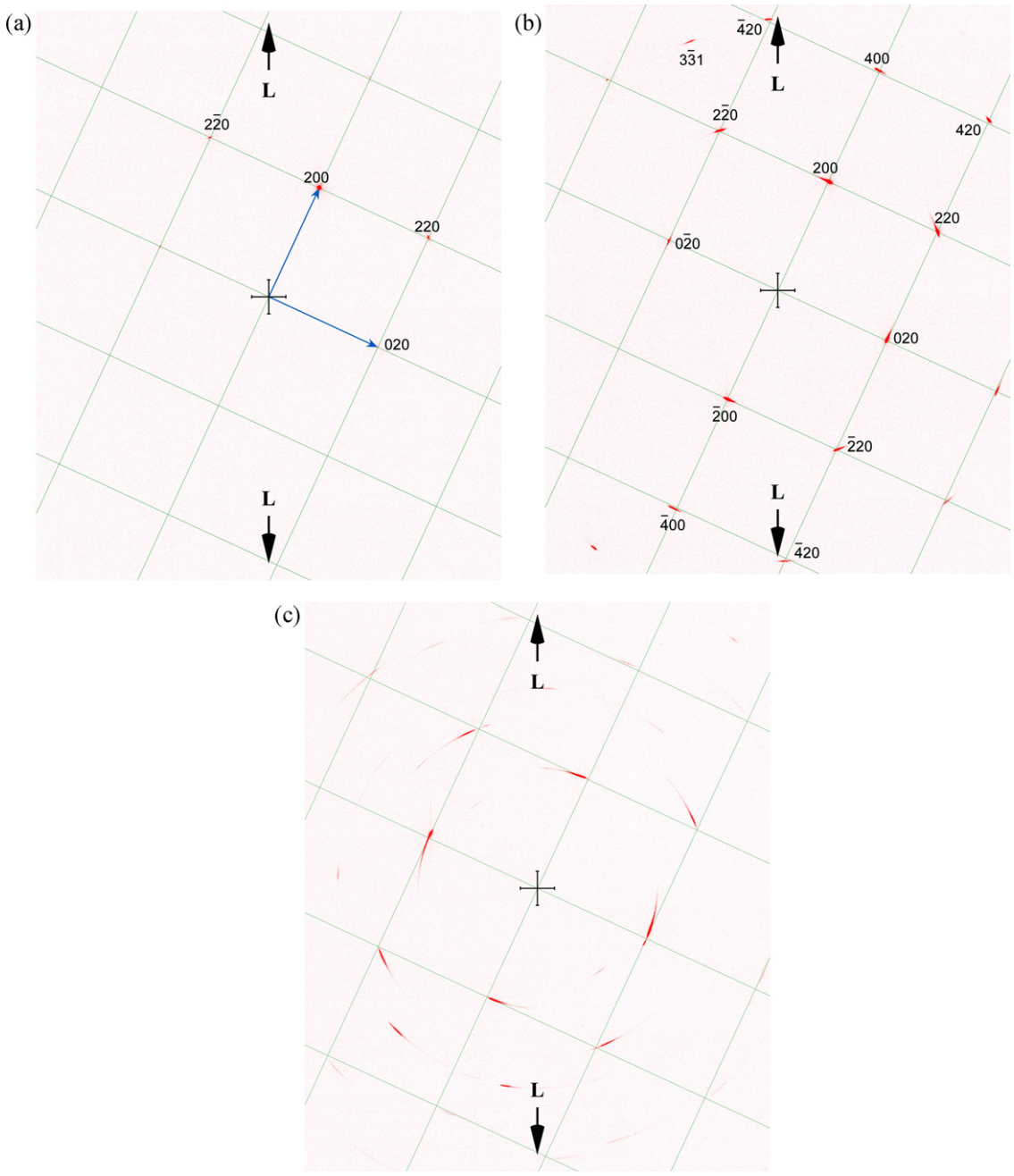

Fig. 6. Two-dimensional diffraction maps for different compression states of single crystalline copper.

Author's personal copy

expected, that not all crystallites fulfill the Laue condition for reflection, i.e. only a smaller number of crystallites have their reciprocal lattice vector **G** matching the Ewald sphere. All the other crystallites do not reflect. It looks like not much was happening in the first 28 s during which the specimen mainly settled between the compression jars. Then, azimuthal peak broadening is observed during which the intensity of the individual spots spreads on the Debye–Scherrer rings. Additional spots appear, mainly between 30 s and 100 s, stemming from reflections which originally were slightly off the Ewald sphere and now getting into the reflection condition due to the same peak broadening effect, which we attribute to subgrain formation and the increase of the mosaic spread of the crystallites. Depending on the orientation with respect to transverse (**T**) and longitudinal (**L**) direction, some of the timelines are inclined, revealing grain rotation around the beam axis due to the plastic deformation process. Eventually, the reflections broaden over many 10° and overlap, merging into the final texture of the material. For an independent check, the global texture of the deformed sample has been measured with neutrons at the QWOKKA instrument of the OPAL reactor [2] and the 1 1 1 polefigure reproduced in Fig. 4. The fiber texture shows a minimum in the **L** direction and two maxima 34° and 90° (=**T**) off the fiber axis, which corresponds well to the intensity distribution at $t = 500$ in Fig. 5a. For clarity, the trace of the reciprocal lattice vector distribution of this Debye–Scherrer ring is indicated in Fig. 4, which is close to a great circle, but parallel off by the Bragg angle of $\theta = \sim 1.9°$. Altogether, the texture approaches asymptotically the distribution known and simulated in literature [10] which would be reached upon infinite, compressive strain and be expressed in a fully symmetric pattern of Fig. 2b along **L**.

The situation has been further investigated upon compression of a single crystalline copper sample, which was wire-cut in an arbitrary direction from a specimen of more than 10 mm grain size. Such a single crystal was equally mounted into the load frame and subsequently pre-aligned by rotation around the vertical axis before compression started. A series of diffraction patterns is shown in Fig. 6. Again, only a very small number of diffraction spots is seen in the initial condition, Fig. 6a. The cross denotes the center of the transmitted beam, the origin of reciprocal space, and the bar lengths of the cross-scales to 1 Å^{-1}. The longitudinal direction **L** for subsequent compression is vertical as indicated. The strongest reflection lies on the Cu-2 0 0 ring with $G_{200} = 3.48$ Å^{-1} and is indexed 2 0 0. Perpendicular lies 0 2 0, spanning the reciprocal lattice of the single crystal and allowing to index all other observed reflections. The so obtained orientation matrix determines the direction of **L** close to a ⟨4 2 0⟩ axis. This highly symmetric reciprocal lattice plane has been selected by the pre-alignment. Reflection 2 0 0 is strongest because it matches best the Ewald sphere, which is tilted by the Bragg angle of $\theta = \sim 2.2°$ towards 2 0 0. The mosaic spread of the crystal is large enough, to match 2 2 0 and 2 −2 0 and weakly 0 2 0, 0 −2 0 and 4 0 0 to the Ewald sphere, while the opposite direction is further off, i.e. −2 0 0 by ∼4.4°. From this we estimate the mosaic spread being less than 2° and indeed, the azimuthal spread of the 2 −2 0 reflection is 1.5°. Fig. 6b shows the situation after compression to $\varepsilon = -0.075$ where many additional reflections of the reciprocal lattice became visible. It is also observed, that the reflections broaden in the azimuthal direction, i.e. they spread out on the Debye–Scherrer rings, to a more or less uniform distribution of up to ∼8°. This is due to the mosaic spread originating from the defects introduced by the plastic deformation process. Well known as such are dislocations and dislocation cells [11], introducing small angle boundaries between the subgrains, forming the mosaic blocks of the single crystal and a characteristic orientation distribution. The situation is demonstrated in Fig. 7 with an incident wave vector $\mathbf{k}_O$ impinging the origin **O** of reciprocal space and a reciprocal lattice vector **G** lying on the Ewald sphere *S* fulfilling the Laue condition

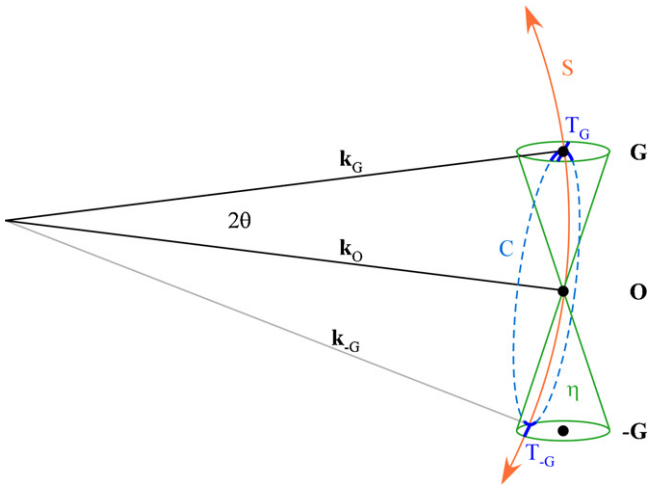

Fig. 7. Reciprocal space construction for diffraction on a mosaic crystal.

$\mathbf{k}_G = \mathbf{k}_O + \mathbf{G}$ for reflection. The opposite reciprocal lattice vector $-\mathbf{G}$, however, lies by 2θ off the Ewald sphere and the reflection is not excited initially. In a powder sample, the scattering vector orientation distribution for the considered reflection would lie on the cone *C* on *S*. As mosaic spread increases within some distribution η around the reciprocal lattice points, scattered wave vectors are excited in the intersection of η with *C* leaving a trace T_G along the Debye–Scherrer ring. In particular, when the mosaic spread overcomes the misalignment of $-\mathbf{G}$, 2θ in this case, the reflection appears with a shorter than maximal trace T_{-G}. More and more reflections subsequently intersect the Ewald sphere according to their distance from it and their geometry in the second dimension. Eventually, reflections like the 3 −3 1 in Fig. 6b, out of the plane spanned by 2 0 0 and 0 2 0 and lying in the third dimension of reciprocal space, intersect and appear. The grain breakage has further evolved at $\varepsilon = -0.15$ in Fig. 6c where the mosaic distribution became more inhomogeneous. Particularly, the azimuthal wings are asymmetric and their centers deviate into a counter-clockwise sense stemming from a rotation of the whole into the direction of preferred deformation orientation.

From the above said, we can now zoom into features appearing in the timelines from Fig. 5 of the polycrystalline copper sample. The 2 2 2 spot at azimuthal-angle $\psi = 90°$, Fig. 5e, reproduced as feature B in Fig. 8c shows smooth broadening, linear with deformation. As in the single crystal case, this corresponds to the formation of subgrains leading to angular distortion of the initially flat and parallel lattice planes of the whole grain. These can be dislocation walls, cells, etc., leading to small angle subgrain boundaries. The mosaic spread increases linearly as a function of time and strain, i.e., the angular distortions add up upon further deformation. Since the subgrains are fine and many in the illuminated volume, they cannot be distinguished in the present setup, however, there may be intensity distributions within the mosaic cone revealing preferred deformation channels. Some reflections appearing later upon progressive deformation, such as around $\psi = 300°$ on 1 1 1, magnified and marked *P* in Fig. 8a, show a hyperbolic rather than linear evolution with time and strain. In this situation, the reflection lies initially off the Ewald sphere as discussed for the single crystal, and appears while the mosaic spread broadens linearly. The intersection of the (locally flat) Ewald sphere with the mosaic cone in angle/time space leads to a conical *C* which is a hyperbola *P* and a linear opening for off-centered and centered reflections, respectively. Concluding this to a first order approximation, angular distortions of the subgrains evolve linearly with deformation in both dimensions of orientation space.

Author's personal copy

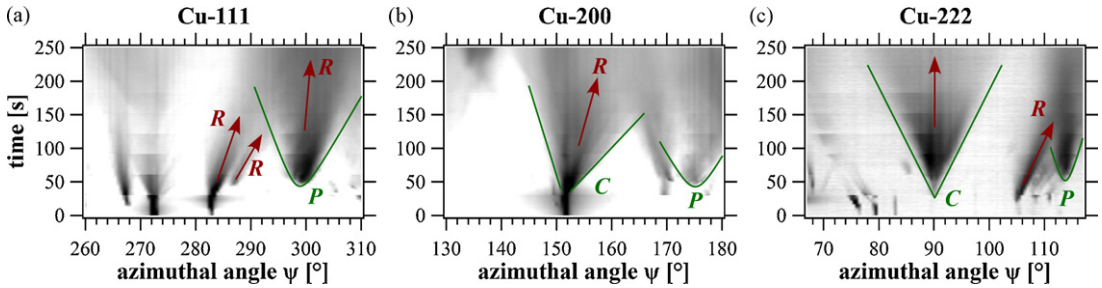

Fig. 8. Magnified extracts from features in Fig. 5, revealing mosaic cones *C*, *P* and grain rotation *R*.

Apart from a few special cases, the timelines are inclined in the azimuthal-angle/time plots. The 2 0 0 reflection at $\psi = 152^\circ$ is magnified in Fig. 8b broadening into a conical *C* as discussed, but asymmetric, resulting in a net shift on the azimuthal-angle scale, which corresponds to a grain rotation *R* projected to a plane perpendicular to the incident X-ray beam. Spots from other grains, such as on 2 2 2 at $\psi = 105^\circ$ and on 1 1 1 at $\psi = 283^\circ$, featured *R* in Fig. 8c and a, show predominant rotation while mosaic broadening occurs on a lesser scale. It may also happen, that the envelope first spreads linearly and then narrows again while the intensity fades away, which is seen for example on 2 0 0 at $\psi = 320^\circ$. In this case, the grain rotates away from the Ewald sphere.

The scenario of the evolution from single grains to texture can be described as following. Initially large (300 μm), near-perfect crystal grains lead to few, sharp spots on the Debye–Scherrer rings. Upon compression, dislocations and dislocation structures are continuously introduced creating angular distortions, so-called mosaic spread, increasing linearly with the plastic strain. The intensity distribution is smooth within the mosaic spread indicating a fine subgrain structure (≤1 μm). Some of the grains rotate conform with slip deformation, depending on their initial orientation with respect to the preferred orientation. Each final texture maximum has a zone of attraction from which the timelines converge. Some special points in orientation space are those, which lie already in a maximum or minimum of the asymptotic texture, leaving such oriented grains in a stable or instable equilibrium, respectively. The rotational stable grains just broaden in mosaic spread and eventually merge into the texture. An example is given on 1 1 1 at $\psi = 54^\circ$ or on 2 2 0 at $\psi = 18^\circ$. Grains in instable orientations, such as on 2 2 2 at $\psi = 90^\circ$ spread extensively in mosaic, caused by slip on the three other {1 1 1} systems and competitive subgrain rotation into the preferred orientation, diluting the intensity in the texture minimum.

4.2. Twinning in magnesium

While dislocation slip on the {1 1 1} planes is the only notable, activated deformation system in the highly symmetric, fcc copper, twinning may play an important role in systems with lower stacking fault energy or in less symmetric systems like hcp lattices. For completeness, we show in Fig. 9 the timelines of the 1 0 1 reflection of polycrystalline magnesium. It qualitatively shows the basic features as discussed on copper for slip deformation, namely spread in mosaic and grain rotation. In addition to that, timelines disappear and others suddenly appear, which is related to twinning. Known twin systems in magnesium occur by mirroring on {1 0 1}, {1 0 2}, {1 0 3} all showing a common ⟨1 −2 0⟩ axis, resulting in large angle reorientation of the reciprocal lattice vectors. In addition, out-of-plane, equivalent reflections can be related by a multitude of different angles and further, double twinning has been reported, such as {1 0 1}–{1 0 2} and {1 0 1}–{1 0 3} for compression mode [12,13], leading to a multitude of crystallographic rearrangements. If a 1 0 1 spot is initially observed on the Debye–Scherrer ring, partial twinning of the grain takes away its intensity, reorienting the corresponding reciprocal lattice vector. For a given initial orientation, the twinned reciprocal lattice vector can appear on a cone around it, defined by the given twin angles. Generally, it will be off the Ewald sphere, so the reflection disappears upon twinning. Similarly, other grains can twin into an orientation matching the Laue condition and suddenly appear. Only in the very special case, that the twinning axis is slightly inclined to the incident beam axis, in such a way, that both initial and twinned reciprocal lattice vectors lie on the Ewald sphere, simultaneous intensity increase of the twin reflection in cost of the initial reflection can be observed. Occasionally, in a polycrystalline material, such situations are observed. Fig. 9 shows indeed such fingerprints. The timelines at $\psi = 107^\circ$ switching to 53° at $t = 50$ s and further to 160° at $t = 300$ s can be explained by {1 0 2} flip of 52.4° correlating

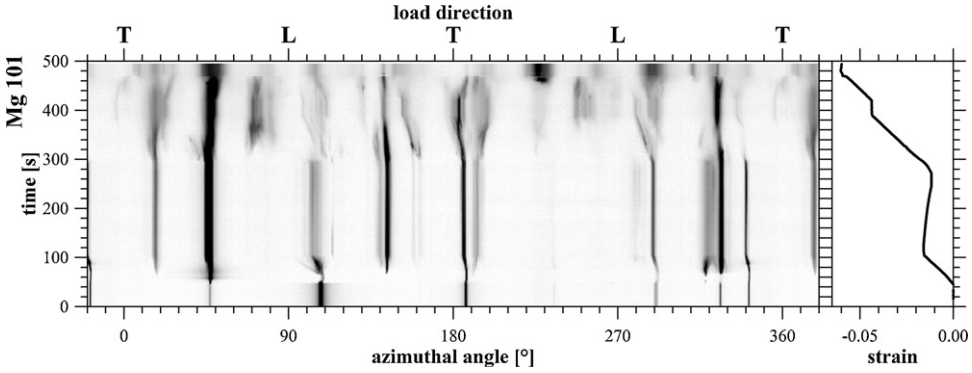

Fig. 9. Azimuthal-angle/time plots for compression of polycrystalline magnesium alloy.

Author's personal copy

$1\,0\,1_{parent}$ and $1\,-1\,1_{twin}$. Short to say, fingerprints of twinning are the sudden changes of timelines from one orientation to another, often superimposed to mosaic broadening and grain rotation. Apart from slight fluctuations due to the individual shear stress distribution, twinning appears simultaneously in many grains suffering similar stress during a plastic deformation process.

4.3. Twinning induced plasticity steel

Different deformation mechanisms can be activated in fcc crystal systems depending on the stacking fault energy. At high energy costs, stacking faults are not introduced and dislocation slip is favored, as previously described in copper. Medium stacking fault energies allow to change the sequence of stacking eventually here and there, leading to twin lattices which themselves show the same crystal structure as the parent, separated by a rare stacking fault as compared to the number of lattice planes. In contrast, low energy costs favor the rearrangement of the stacking sequence on the scale of each atomic plane which is a martensitic phase transformation.

Stacking fault energies may be altered by the chemical composition of alloying elements. This is widely applied in steels, which are probably the major materials used for structural components. Applications of steels are extremely wide and mechanical properties range from hard and brittle to soft and ductile. Much effort is driven to develop steels of both high strength and ductility, desired to reduce weight by thinner materials; and good response and safety to impact, such as in the car and transportation industry. One of the newer developments are twinning induced plasticity steels of the fcc austenitic phase, which are intrinsically hard and simultaneously respond plastically to external load by a twinning deformation process.

A twinning induced plasticity steel with the composition Fe–25Mn–3Si–3Al (wt.%) has been tested in situ during a tensile test on the beamline ID15B [3]. Dog-bone specimens of 1 mm width and 15 mm gauge lengths were prepared by wire cutting from a 2.5 mm thick, hot-rolled sheet, perpendicular to the rolling direction. The initial, average grain size was determined to 20 μm. Azimuthal-angle/time plots are shown in Fig. 10a and b for the 1 1 1 and 2 0 0 reflections. They show the initially relatively coarse

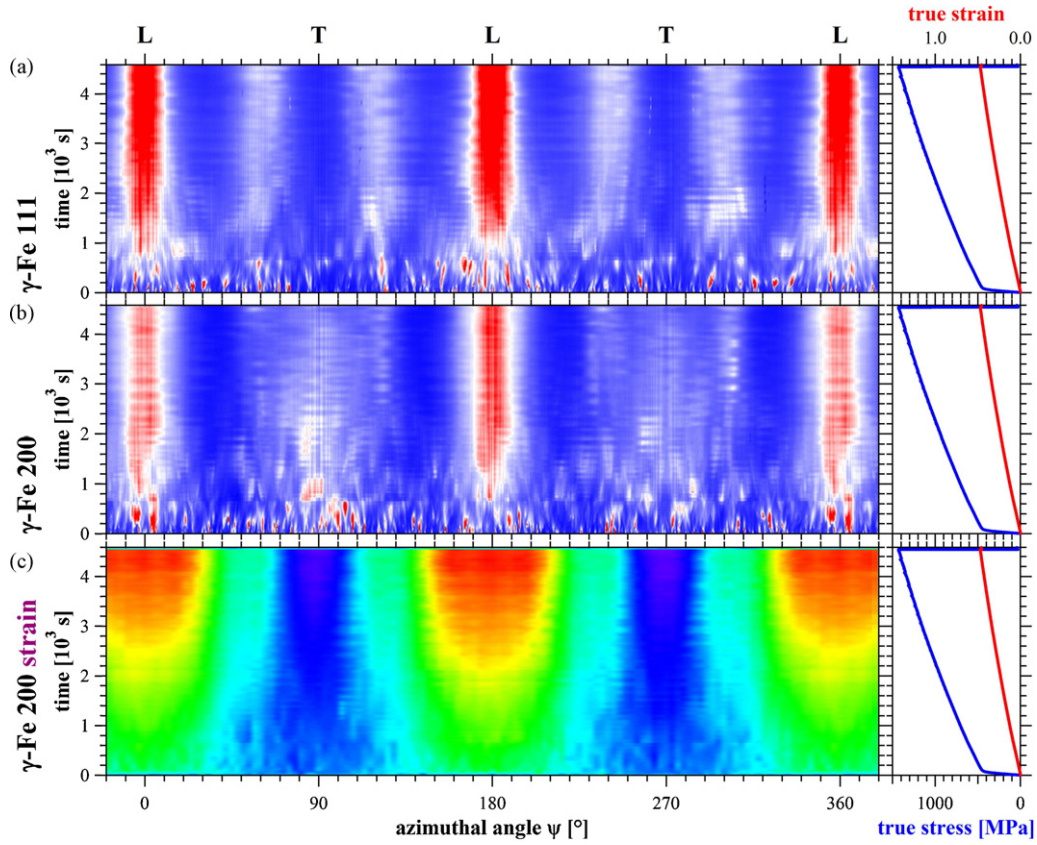

Fig. 10. Azimuthal-angle/time plots for twinning induced plasticity steel undergoing tensile testing (a and b); Strain map of the 2 0 0 reflection (c).

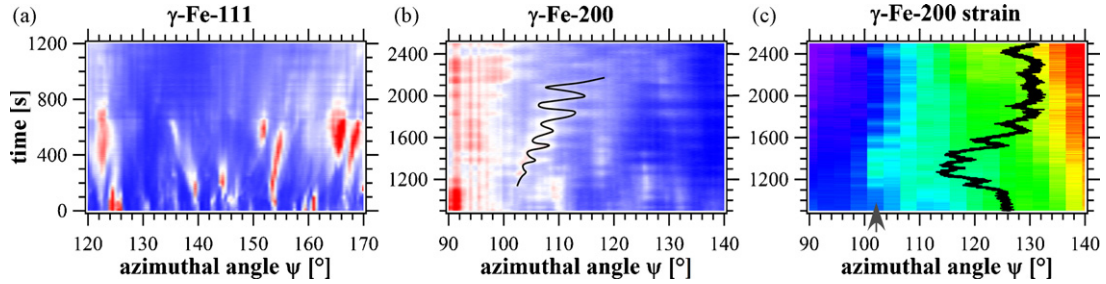

Fig. 11. Magnified extracts from features in Fig. 10, revealing initial twinning (a), intensity oscillations (b) and strain oscillations (c).

Author's personal copy

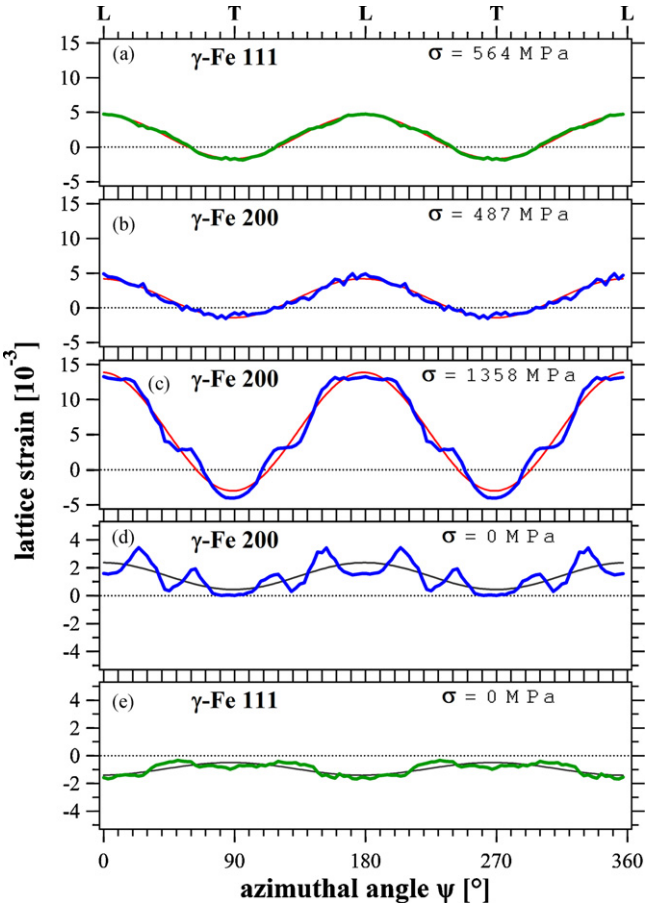

Fig. 12. Lattice strain distribution in twinning induced plasticity steel undergoing tensile testing for selected reflections upon loading (a–c) and unloading (d and e).

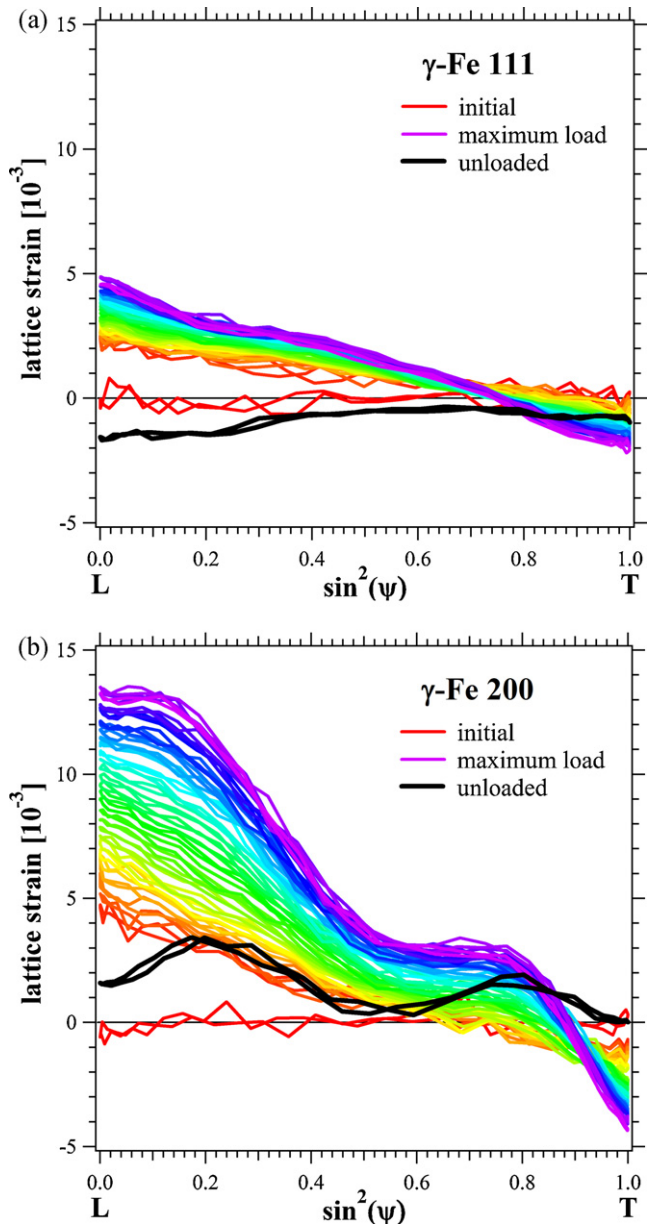

Fig. 13. $\mathrm{Sin}^2(\psi)$-plots for selected reflections in twinning induced plasticity steel.

grain undergoing mosaic broadening and grain rotation. On top of this, twinning occurs as recognized by the disappearance of initial, together with the appearance of new timelines, Fig. 11a. After grains have fully twinned for the first time, they are in their energetically favorable state and would not twin back under continuous load and must further deform though dislocation slide as seen by further increase of the mosaic spread and the increase of texture. After the grain has rotated, cross-twinning on other {1 1 1} planes is activated, and eventually competition and interplay between the two deformation mechanisms takes place in an oscillatory behavior, as seen in the temporal coming and going of intensities in a given orientation in azimuthal-angle/time plot, Fig. 11b. Note, in some crystallographically distinguished orientations, as 1 1 1 along **L**, or 2 0 0 along **L** and ±54°, the timelines just oscillate, while they form zigzag lines on less symmetric directions (Fig. 11b). Those timelines stem from many fine grains, which oscillate in a collective behavior. The zigzag lines form, when gradually oriented grains successively enter the critical shear stress to twin. The 1 1 1 texture sharpens and converges dramatically because the 1 1 1 orientations of the twins matches closely the polefigure of a pure slip deformation texture in a fcc system [10]. Not so the 2 0 0 orientations, which are twinned into regions of the pole figure, where a pure deformation texture is far from its distribution maximum. This is consistent with the large fluctuations underlying the twinning oscillations observed in Fig. 10a and b. The strain orientation map is obtained from the radius of the Debye–Scherrer rings and plotted in Figs. 10c and 11c for the 2 0 0 reflection while line cuts at given times are reproduced for 1 1 1 and 2 0 0 in Fig. 12. As expected under tensile load, the elastic strain increases along **L** and decreases through the Poisson effect across **T**. The strain partitioning over the differently oriented grains has been evaluated and modeled along these main directions [3], however, more information is obtained when regarding the full anisotropy of the strain. An elastically isotropic medium would show a sinusoidal behavior in azimuthal-angle, describing the strain ellipsoid. In such a case, strain ε plotted vs $\sin^2(\psi)$ results in a straight line, which is pretty much the case for the 1 1 1 orientation, reproduced in Fig. 13a. At low stress, 2 0 0, shown in Fig. 13b behaves similarly sinusoidal, but then forms a plateau between $\sin^2(\psi) \in \{0, \ldots, 0.12; 0.5, \ldots, 0.8\}$, $\psi \in \{0, \ldots, 20^\circ; 30^\circ, \ldots, 54^\circ\}$. This we attribute to the relaxation of shear stress by twinning, which is accumulated, when pulling a grain along (2 0 0) leading to shear stress on (1 1 1). Once overcoming the critical shear stress, twinning occurs relaxing the lattice strain around **L**. The equivalently observed, out-of-plane 0 2 0 reflection of the relaxing lattice then flips by 48° contributing to the second plateau in the slope of the sinusoidal curve. Upon unloading, this inhomogeneous and anisotropic strain distribution results in complicated residual stresses (Fig. 12d and e) and explains a large springback effect which has already been predicted [14].

Author's personal copy

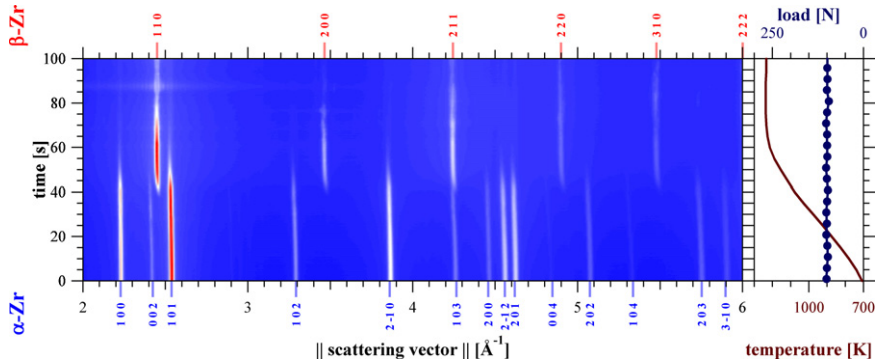

Fig. 14. Powder diffraction patterns of Zircaloy-4 revealing the phase transformation.

4.4. Hot plastic deformation

So far, we presented diffraction results undergoing mechanical processing at room temperature. The evaluation of 2D diffraction patterns allows to read and distinguish grain size, grain perfection, subgrain formation, grain refinement, grain rotation, grain orientation relationships, texture evolution, strain and strain anisotropy which can be correlated to slip deformation and twinning. At elevated temperatures, however, thermally driven phenomena of which the most important are phase transformations, grain growth, recovery and recrystallization, play an important role. Upon additional plastic deformation, these different processes become dynamic in their characteristics, interplaying or competing with each other. The following chapters will present these aspects on examples, obtained from zirconium alloy and titanium aluminium based intermetallics.

4.5. Zirconium alloy under hot, tensile testing

Zirconium alloys play an important role in the nuclear reactor and waste technology, as they combine neutron transparency with good resistance to radiation damage. They are employed, for example, as fuel cladding and as structural engineering materials in reactor designs. Here, we elaborated tensile specimens of 6 mm × 5 mm cross-section from hot-rolled sheet of Zircaloy-4 grade R60804 of nominal composition Zr–1.5Sn–0.2Fe–0.1Cr–0.1O (wt.%). The phase diagram shows a hexagonal closed packed (hcp) α-Zr structure below 1083 K and a body centered cubic (bcc) β-Zr structure above 1253 K [15]. The specimen underwent a multitude of heating/cooling cycles from the α- into the β-phase, each with different applied, constant load while diffraction data was recorded. Fig. 14 shows the azimuthally integrated powder diffraction patterns as a function of momentum transfer and time during the first heating ramp depicted on the right, revealing the phase transformation α → β. As temperature increases, the α-reflections cease away in favor of the β-lines. The process also shows the phase coexistence of both in a finite temperature regime. Those in situ powder diffraction data are the basis for quantitative phase analysis and detailed studies of the lattice parameters, which not only vary on thermal expansion but may show anomalies due to variation in chemical composition, order and disorder and more [16–19]. Typical original 2D diffraction patterns below, during and above the phase transformation and for both the first and the last heating ramps are depicted in Fig. 15. The applied constant external load was 100 N and 225 N, respectively. Azimuthal-angle/time plots for selected reflections are produced in Fig. 16a and b. Initially, the grain size of the prepared materials was determined to be 20 μm [20], representing a fine, but well distinguished distribution of spots on the Debye–Scherrer rings of the initial α-phase, Fig. 15a. Apart from the spottiness, there is texture which can be seen particularly well by the anisotropic intensity distribution on the α-0 0 2 ring, which is apparent along the **T** direction and missing along **L**. Other reflections, such as the α-1 0 1 appear more isotropic due to the higher multiplicity, being 2 and 12, respectively for both reflections. The azimuthal-angle/time plot in Fig. 16a and b shows by the static behavior of the timelines, that the microstructure does not change at lower temperatures. Starting in the regime around 1000 K, fluctuations and some coarsening take place which we attribute to the relaxation driven by internal, residual stresses in the material. Reaching the phase transformation, the β-rings appear, Figs. 14, 15b and 16b, smooth and continuously, telling of a very fine and randomly oriented microstructure. Also the α-rings smoothen before they disappear upon transformation, more likely due to mosaic broadening rather than grain refinement. Through orientation relationships, texture is inherited in the β-phase, expressed by the higher intensity distribution along **T** and **T** ± 48°, Fig. 16c. The timelines of the β-phase fluctuate and eventually coarsen while the lesser number of lines increase in intensity, Fig. 16b, which is due to rearrangements of the microstructure, such as recovery, and grain growth, ending up with only a small number of reflections in Fig. 15c. At this stage we know, that grain has grown probably to ∼200 μm size, which then evolved into a Widmanstätten growth of α-phase on subsequent cooling and finally transformed back into a pure α-phase as shown in Fig. 15d [20]. After transformation, the α-reflections are considerably broader than the high temperature β-reflections. Indeed, the latter widen when the α-phase nucleates and grows due to the misfit of the phase coherency in the Widmanstätten-like microstructure. The forward and backward transformation and the according microstructure are mostly reproducible when cycling multiple times through the phase transformation. Initially established variants of the orientation relationships are pretty much conserved on the investigated time scales and negligible external load. This has been verified with a zero load heating/cooling cycle prior to the last heating ramp presented in the 2D diffraction patterns of Figs. 15d–f and the azimuthal-angle/time plots from Fig. 17. As discussed, there exists only α-phase with large grains of ∼200 μm showing broad mosaic spread of typical 4° leading to a decent occupation on the Debye–Scherrer rings, the number of spots being proportional to the multiplicity {6, 2, 12} of the reflections {1 0 0, 0 0 2, 1 0 1}, respectively. In the two-phase field, β-reflections appear, such as β-1 1 0 lying in the narrow gap between the α-0 0 2 and the α-1 0 1 rings, which themselves have sharpened slightly in mosaic spread. The β-1 1 0 reflections are 1:1 aligned in azimuthal-angle with α-0 0 2, which fulfills the condition for a Burgers orientation correlation $(0\,0\,1)_{hcp}||(0\,1\,1)_{bcc}$, $[2\,-1\,0]_{hcp}||[1\,-1\,1]_{bcc}$ [21,22]. There is another observed relationship, almost each β-1 1 0 matching an α-1 0 1 which is the condition for the Potter orientation correlation $(0\,0\,1)_{hcp}$ 2° off $(0\,1\,1)_{bcc}$, $(0\,1\,1)_{hcp}||(1\,1\,0)_{bcc}$, $[2\,-1\,0]_{hcp}||[1\,-1\,1]_{bcc}$. Indeed, some α-0 0 2 reflections are shifted azimuthally

Author's personal copy

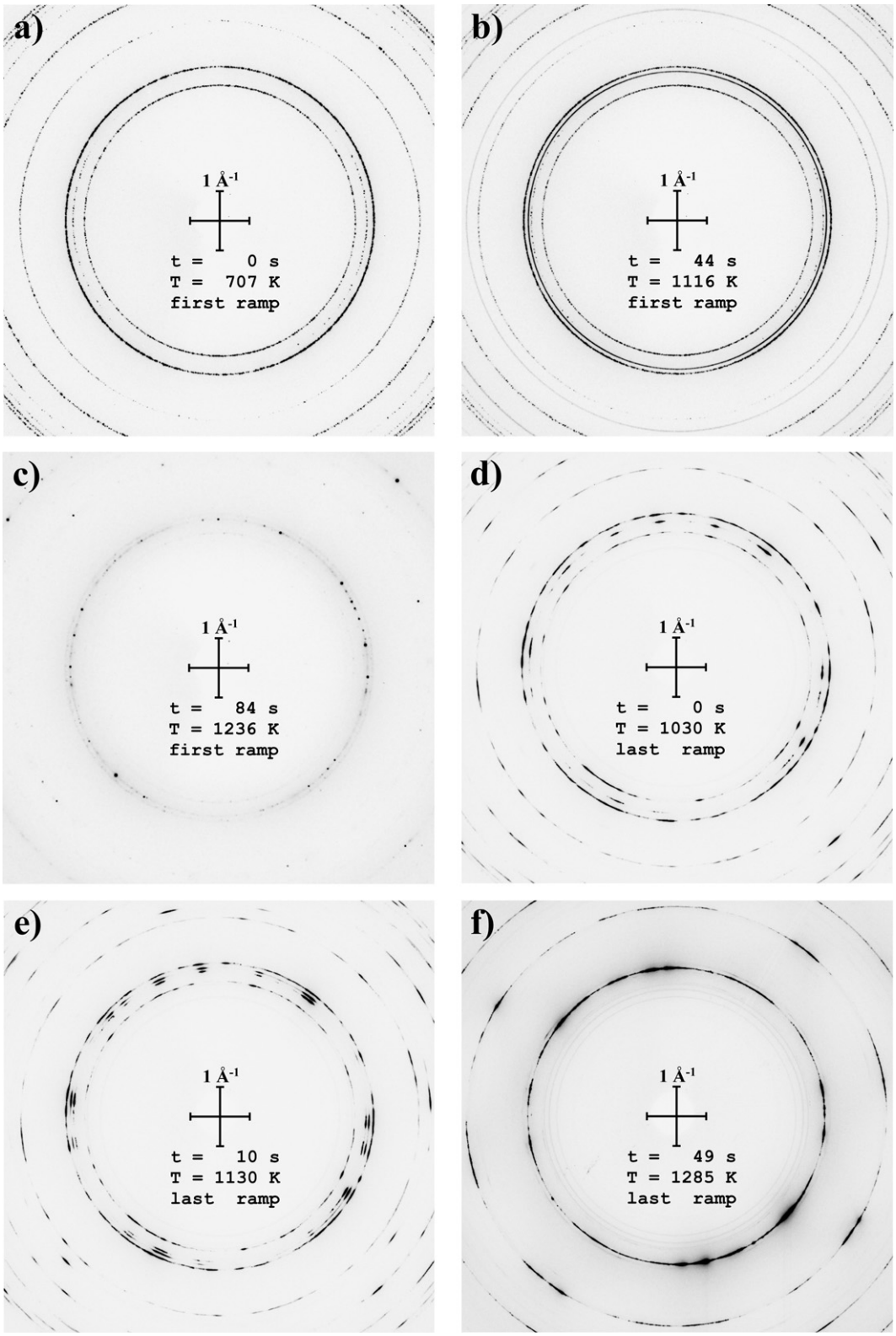

Fig. 15. Two-dimensional diffraction patterns from Zircaloy-4 during thermo-mechanic deformation on two temperature ramps.

up to 2° towards β-1 1 0. Reversing the transformation in thoughts or experimentally, this leads to preferred grain orientation relationships in the α-phase, expressed by the correlated grouping of intensities on the α-0 0 2, α-1 0 1 and to some extend the α-1 0 0 rings. On such almost matching lattice plane spacings, together with orientation matching has been previously reported upon preferred grain growth mechanisms in an TiAl α-phase [23].

As temperature increases the phases have fully transformed and the α-reflections disappear. From then on, there is unhindered grain recovery and growth as expressed by the narrowing end-

Author's personal copy

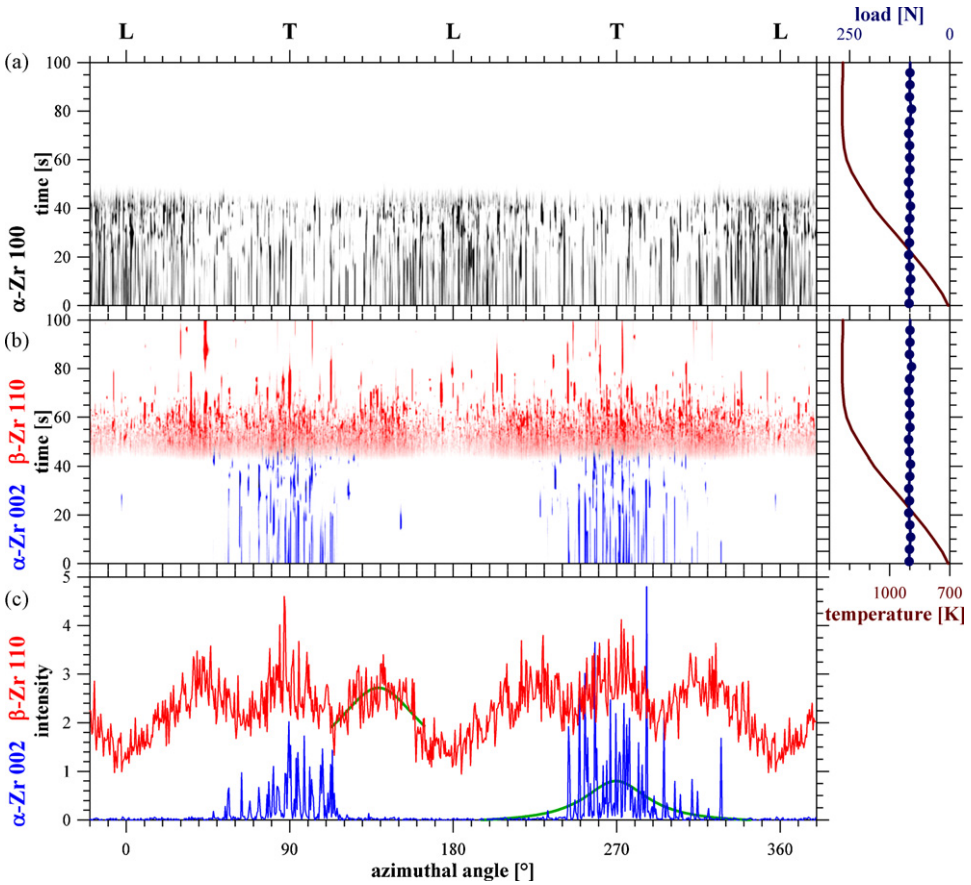

Fig. 16. Azimuthal-angle/time plots of Zircaloy-4 during thermo-mechanic deformation on the first heat ramp.

ing timelines between $t = 20$ s and $t = 30$ s. Eventually, the material becomes soft enough to deform plastically. Other than in cold deformation, there is no smooth spreading of the mosaic distribution, nor large amount of grain rotation. The timelines rather spread into dots which are distributed by a narrow, conical envelope *C*, as reproduced in Fig. 18. Similar than on cold material, mechanical deformation introduces lattice defects, such as dislocation, forming subgrain cells. However, the high temperature facilitates recovery, where dislocations annihilate and neighbor cells grow to a more perfect subgrain. This may occur simultaneously in different regions of the parent grain, leading to a very similar orientation but eventually leaving a small angle boundary between neighboring perfect subgrains. The perfection of the subgrain is expressed by the narrowness of the timeline—the fine-structure of the spottiness in azimuthal-angle, while the small angle grain boundaries are given by the number of coexistent, fine timelines shifted by only fractions of a degree to one or two. As there is continuous competition between the grain breaking and grain recovering process, the fine time lines are very short and fluctuate as appearing dots within their grain's timeline envelope—we call it dottiness. This regime is dynamic recovery.

As deformation in this overall constant-force experiment continues by dynamic recovery, necking occurs, which reduces the specimen's cross-section and effectively alters the actual load on the material, leading to higher and higher deformation rates. At some stage around $t = 35$ s, dynamic recovery becomes unstable and timeline islands appear more or less randomly in azimuthal-angle/time space. An arbitrary rearrangement of large angles is attributed to dynamic recrystallization, where new crystallites grow from a strongly distorted parent lattice. It is obvious, that the subgrain orientation distribution spreads quickly and shows fingerprints of dynamic recovery until they have spread so widely that again recrystallization occurs. Interestingly, the procedure is not fully random. New and neighboring grain orientations, timeline islands, show jumps of the order of 10°, depending on the reflection, and thus the projection observed. Along β-2 0 0, Fig. 17c and trace X (18a), subsequent dynamic recrystallization steps seem to rotate the grain very quickly into some preferred orientation. Altogether, grain refinement competing with thermally driven grain growth occurs, showing a more continuous illumination of the Debye–Scherrer rings than in the static case, Fig. 15f and c, respectively.

Finally, the sample failed by rupture when the load dropped at $t = 49$ s and the driving force for grain refinement was lost, expressed by more and more coarsening, less fluctuating timelines showing static recovery and finally grain growth.

4.6. Hot compression of titanium aluminium

Analogous to zirconium, titanium alloys show similar phase transformations between the hcp and bcc structures. High alloying, however, forms intermetallic compounds which may be ordered and stable to very high temperatures, accompanied by rather complicated phase diagrams presenting often multiple-phase fields. Due to the good high-temperature mechanical properties, oxidation resistance and high specific strengths, γ-based titanium aluminium is since long in the focus of applied alloy design. The main drawback, however, is the narrow deformation window, under which thermo-mechanical processing can take place, mostly in the α-phase with the drawback of deformation in a hexagonal structure, such as limited deformation systems, strong anisotropy and texture development. In addition, the single α-

Author's personal copy

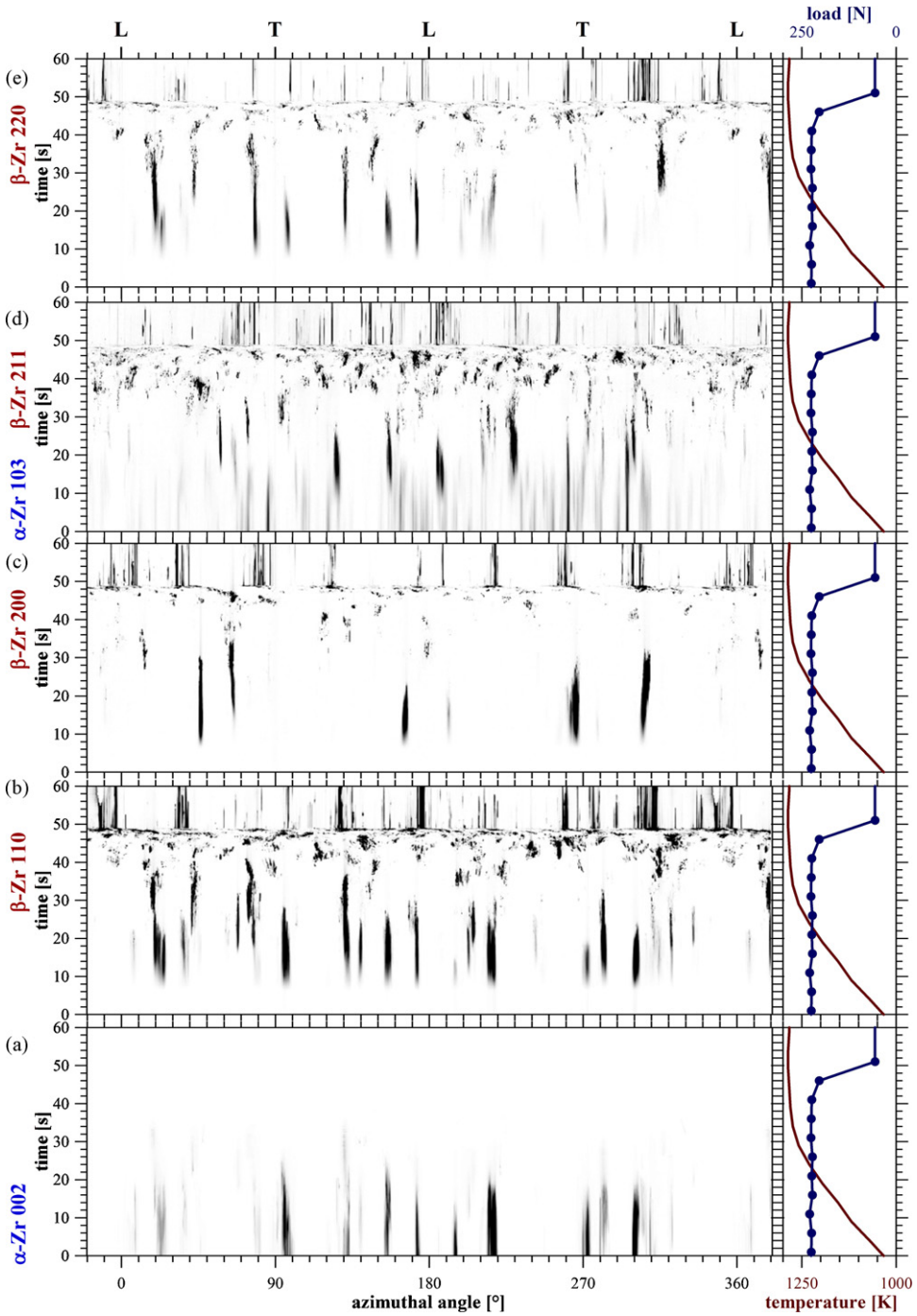

Fig. 17. Azimuthal-angle/time plots of Zircaloy-4 during thermo-mechanic deformation on the last heat ramp.

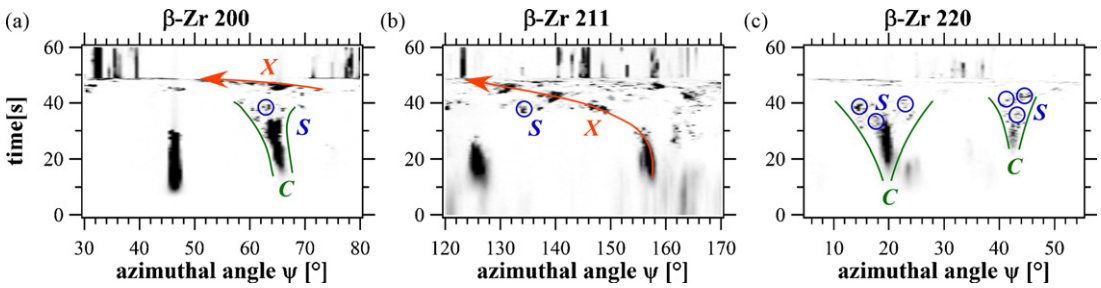

Fig. 18. Magnified extracts from features in Fig. 17, revealing mosaic cones *C*, dynamic recovery *S* and dynamic recrystallization *X*.

Author's personal copy

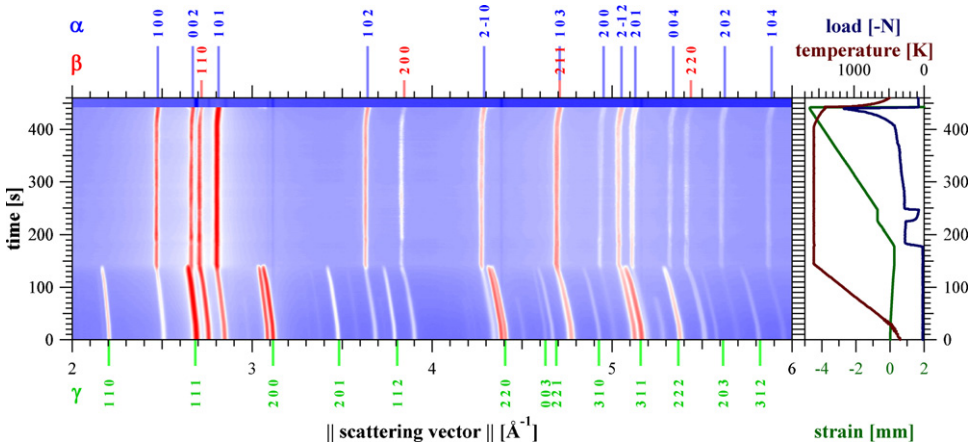

Fig. 19. Powder diffraction patterns of TNM™ revealing the phase transformation and thermal expansion.

phase above ~1570 K shows huge grain growth effects while a coexistent α + γ phase field above ~1450 K suffers from brittleness and slow deformation rates. Therefore, modern alloy design goes into the direction to stabilize the bcc β-phase, particularly at deformation temperatures. This phase is known to have excellent and isotropic deformation properties. A particular compound is so-called TNM™ alloy of nominal composition Ti–43.5Al–4Nb–1Mo–0.1B (at.%) which exposes all three phases, near-fcc γ of ordered $L1_0$ structure, hcp α- and bcc β-phase [24]. At low and operating temperatures, those latter phases can be ordered [19] and lead to further restrictions of deformation mechanisms and increasing strength of the material. For the present hot compression study, it is important to know, that α + β + γ-phase coexist at low temperatures with only little amount of β, while the γ-phase vanishes at the alpha transus temperature T_α, leaving an increasing abundance of β in α material.

Azimuthally integrated diffraction patterns are presented in Fig. 19 as a function of momentum transfer and time, together with the thermo-mechanical process parameters to the right. The disappearance of the γ-phase in favor for α-phase is clearly seen at T_α = 1555 K which is in very good agreement with T_α reported in literature [19,25]. Three selected 2D diffraction images are compiled in sectors of Fig. 20, prior to deformation, below and above T_α (a and b) and while undergoing plastic deformation (c). Fig. 20a shows still all three phases, as indexed in Fig. 19. Like in the case of zirconium treated above, there are orientation relationships between the phases, particularly seen in the dotted frame in Fig. 20a. Both the Burgers and the Potter orientation relationships occur between the α- and the β-phase which can be seen by reflections matching α-0 0 2 with β-1 1 0 and matching β-1 1 0 with α-1 0 1, respectively. In titanium aluminium, the γ-1 1 1 reflection always overlaps with the α-0 0 2 reflection (see also Fig. 19), the Blackburn orientation correlation [26], which favors the typical lamellar microstructure of this compound. In a first order approximation, these two phases just differ by change of their stacking sequence from fcc and hcp, respectively and transform into each other by a displacive mechanism, while a comprehensive description involves diffusional rearrangements to adjust the atomic order driving towards the stoichiometry γ-TiAl and α_2-Ti_3Al. The slight tetragonal deviation of the γ-structure from the fcc lattice leads to splitting of the γ-0 0 2/γ-2 0 0 reflection, on which we observe similar intensity correlations appearing opposite to each other. It has been shown, that this relates to domain correlations within one γ-lamella or between different γ-lamellae coupled coherently by an α-lamella with the above said Blackburn correlation [23]. Last not least, there is a correlation between the γ-0 0 2/γ-2 0 0 pair, the α-1 0 1 and α-1 0 0 reflection, which has been observed to transform into each other through a straight line [27]. To our knowledge, the present observation reports for the first time on the coherent orientation correlations between all three phases and their transformations, mentioned and published in [5].

The γ-phase has disappeared in Fig. 20b and abruptly in Fig. 19 when T_α is passed. The γ-1 1 1 timelines end in the azimuthal-angle/time plot in favor of strong intensity increase in α-1 0 0 and α-1 0 1, according to the phase transformation. It is worth to note, that all α-timelines remain stable in reflection condition, appearing as straight, vertical lines, even while holding the temperature above T_α, until external load is applied and only small fluctuations are observed in the minority β-phase. This proves, that the α + γ lamellar structure transforms fully coherently through the above mentioned orientation correlations from colonies into α-grains of equal size and shape, while the surrounding β-grains are minimal affected from this transformation. The timelines of the overlapping

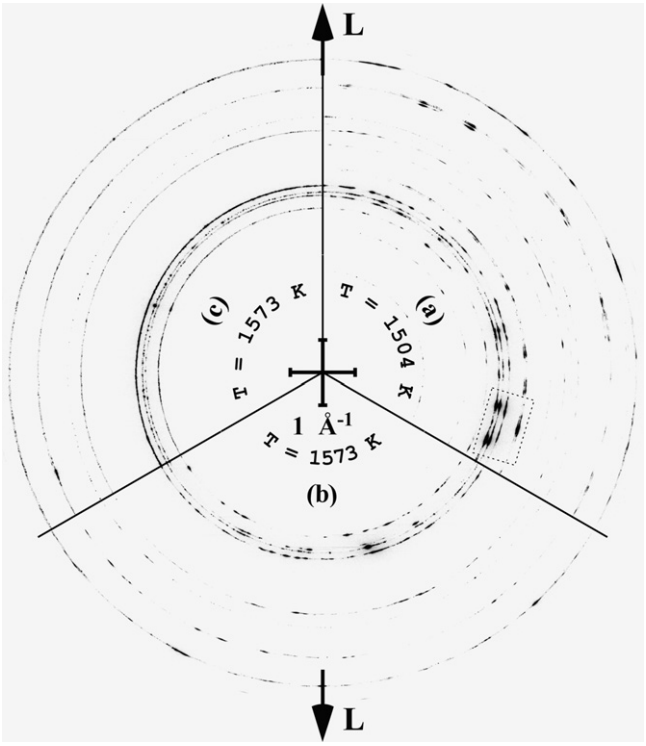

Fig. 20. Two-dimensional diffraction patterns from TNM™ during thermo-mechanic deformation.

Author's personal copy

α-0 0 2/γ-1 1 1 rings show the ending γ-timelines while individual α-timelines can be followed from the beginning throughout the whole heating ramp. With high certitude, those continuous timelines are the superposition of intensity reflected from both α-0 0 2 and γ-1 1 1 lamella correlated by the Blackburn relationship. As the γ-phase decreases by the same amount as α-phase increases, the intensity of the timeline is conserved. From a different point of view, each of the lattice planes reflects a certain amount of intensity regardless of the change in stacking sequence being altered upon transformation. The disappearance of many γ-1 1 1 timelines, not transforming into α-0 0 2 is explained by the decrease of multiplicity from 6 to 2, respectively, and strong variant selection as imposed by the lamellar colony. Therefore, the overall scattered signal has to appear in other α-reflections, such as α-1 0 0 and α-1 0 1, where intensity increases abruptly, without creating new timelines, altogether underlining the full coherence and self-consistency of the phase transformation.

Compression was started at $t = 178$ s after reaching and holding for 34 s the processing temperature of 1573 K, see parameters in Fig. 21. The grain quickly refines as can be seen from the comparison of Fig. 20b and c. It is striking, that timelines for the coexistent α- and β-phase are fundamentally different. The former showing

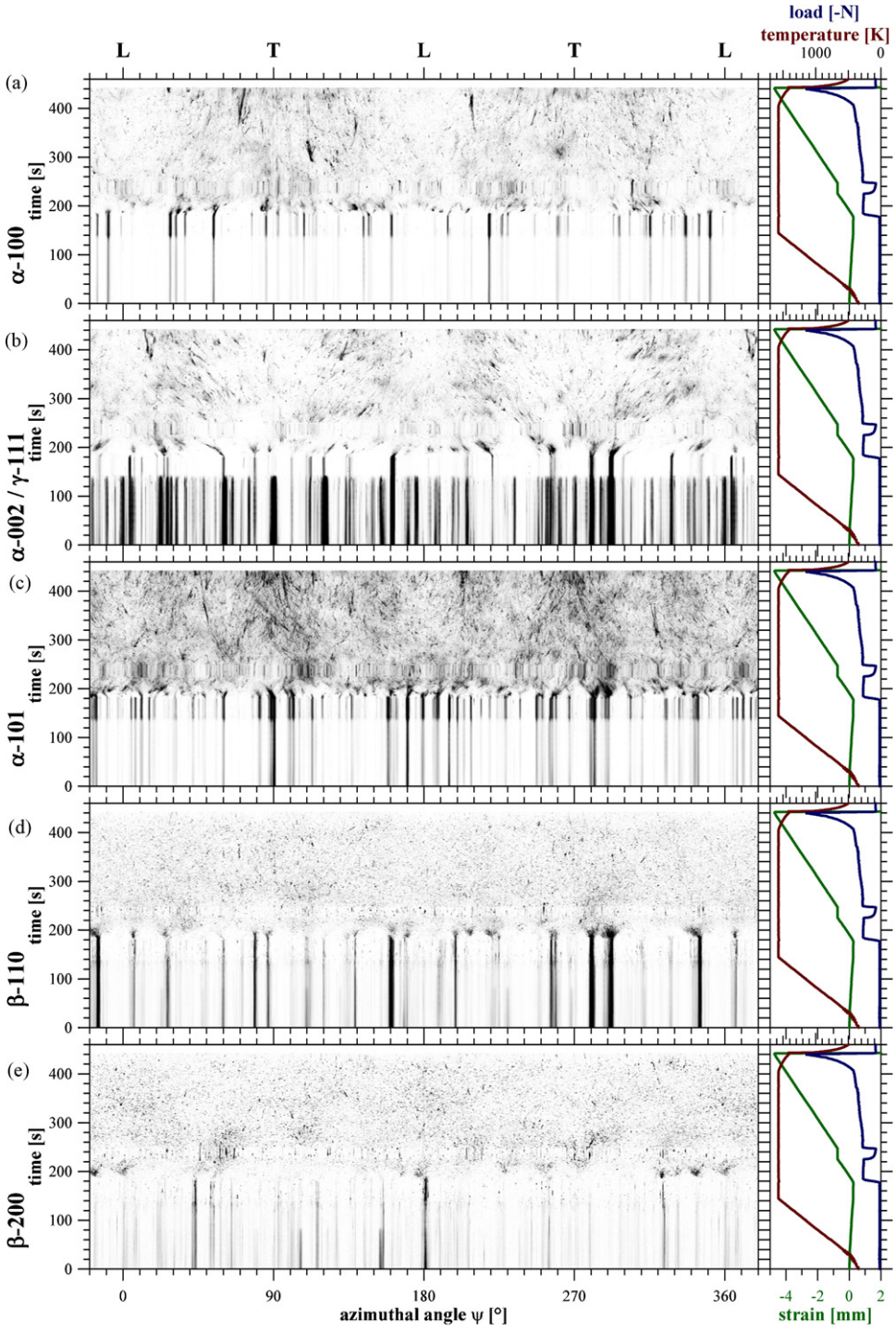

Fig. 21. Azimuthal-angle/time plots of TNM™ during thermo-mechanic deformation.

Author's personal copy

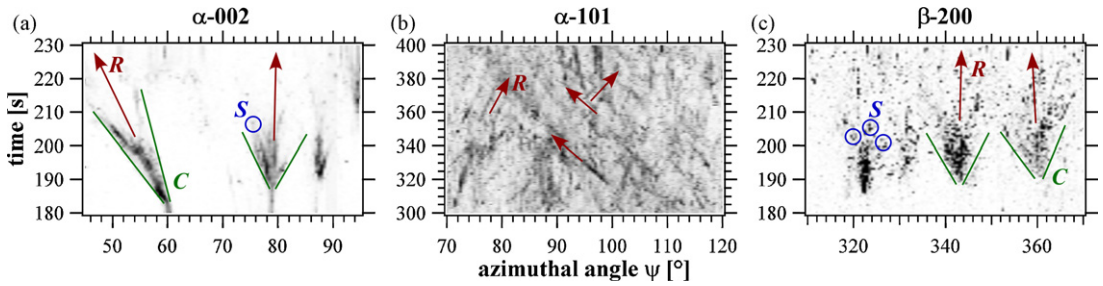

Fig. 22. Magnified extracts from features in Fig. 21, revealing mosaic cones *C*, grain rotation *R* and dynamic recovery *S*.

features as described above in the room temperature deformation processes of Cu, Mg and steel, namely mosaic broadening, grain rotation and the formation of texture, indicating dislocation slip as the primary deformation process. On top of this, there is some blurred dottiness in the timelines, Figs. 21 and 22, stemming from slow dynamic recovery and finally, islands in azimuthal-angle/time space tell of some even slower, dynamic recrystallization. The β-phase, in contrast, shows a rapid spreading of the timelines into a dotted distribution, initially enveloped by a mosaic cone, but then merging and distributing over all orientations. The rapid spread is telling of a high deformation rate while the high density of dots indicate activity of high dynamic recovery, underlined by the only very little evolution of texture. For the present example, the occurring deformation processes have been verified ex situ by electron backscatter diffraction and published elsewhere [28].

The scenario of the α + β-system on progressing deformation is as follows. The α-phase deforms primarily by dislocation slip, leading to a large grain distortion and subgrain structure, which slowly recover. Eventually, lattice distortions build up to that amount to facilitate even slower dynamic recrystallization. The minority β-phase dynamically recovers much faster and can therefore accommodate much higher strain rates holding the α-grains and thus the material together during a ductile deformation process.

5. Conclusion

In situ, real time high-energy synchrotron X-ray diffraction is a powerful tool characterizing the evolution of polycrystalline material undergoing thermo mechanic processing. The different samples systems presented reveal and demonstrate the major deformation mechanisms and consequences related to the microstructure and orientation distribution of the systems, as they can be read from 2D high-energy X-ray diffraction patterns. The major key points are

- Grain size, given by the overall distribution of the spots on a Debye–Scherrer ring. Coarse and fine grains lead to low and high numbers of spots, respectively. In particular, grain refinement or grain coarsening are dynamic effects occurring under thermo-mechanical processing. Care must be taken to calibrate the absolute grain size, as it further depends on the mosaic spread of a grain and the illuminated volume of the specimen.
- Mosaic spread, obtained by the azimuthal-angle distribution of a diffraction spot from one grain. It is a measure for the perfection or the distortion of a grain related to angular distortions stemming i.e. from dislocations and subgrain boundaries.
- Grain rotation, seen by the inclination of timelines in the azimuthal-angle/time plots, which is equivalent to the motion of diffraction spots on the Debye–Scherrer rings. Such grain rotations accompany slip deformation processes and, depending on their starting orientation, point towards the texture maxima for this deformation process.
- Twinning, seen by sudden ceasing of intensity of individual spots on the Debye–Scherrer rings, particularly when others simultaneously appear within a the twinning orientation relationship. Further, twinning can be observed by collective rearrangement of orientation distributions averaged over many grains, as this is known from twinning texture analysis. Fine details, such as the competition of twinning and slip in a system can be seen and elaborated.
- Dynamic recovery, expressed by a lesser overall mosaic broadening and the appearance of sharp dots or short time lines within this envelope, strongly depending on the deformation rate.
- Dynamic recrystallization, observed by larger jumps of several 10° in orientation space, forming islands in orientation space, characterized by a mosaic envelope and dynamic recovery therein.
- Strain and strain anisotropy, evaluated from the eccentricity of the Debye–Scherrer rings and deviation from ellipsoid, best seen in $\sin^2(\psi)$ plots. Under certain conditions, they can be evaluated on a grain scale.
- Individual assessment of different, co-existing phases with respect to all of the above, by reading the information accordingly from the individual Debye–Scherrer rings of each phase.
- Phase fractions by azimuthal integration of the Debye–Scherrer rings leading to conventional in situ phase analysis.
- Grain orientation relationships as on phase transformations and variant selection or during grain growth, nucleation, recrystallization by evaluation of the intensity distributions on the different rings, related by crystallographic aspects.
- Combination of all of the above which may occur simultaneously and where one factor is the consequence of the other.

6. Outlook into the future

The methodology of time-resolved in situ, multi-dimensional high energy X-ray diffraction has now been well established for the characterization of polycrystalline material undergoing structural changes, such as under thermo-mechanical processing. In particular, information is obtained immediately, while such processes occur and makes this method infinitely faster than the conventional method of processing, quenching, cutting, analysis. Nowadays, large area, 2D detectors with few 10 ms time resolution and high pixel-resolution are readily available while developments into the sub-millisecond time scale are ready in the near future. On the other hand, undulators for high energy X-rays to be installed on high electron-energy synchrotron sources now come from the shelves. Therefore, dedicated industrial thermo-mechanic simulation is the next step to be realized by steel manufacturers and other metallurgical industries. The experimental setup is extraordinary simple and more complicated environments, simulating rolling or extrusion shall be envisaged. Investigations under industrial or operating conditions would already be possible nowadays, when the testing equipment was installed at a beamline. An end of devel-

Author's personal copy

opment on both source and detector side is not in sight. Snapshots on ultrashort time scales have already been taken during shock wave compression [29,30], while full movies investigating in situ dynamic loading should be feasible within the next decade [31].

Acknowledgements

We like to thank our collaborators R. Dippenaar, H. Clemens, H. Li, R.P. Harrison, U. Garbe, M. Reid, T. Schambron, D.G. Carr, J. Daniels, O. Kirstein, J.D. Almer, T. Buslaps, M.D. Callaghan, M. Peel for providing the materials, experimental support and constructive discussions.

Access to the APS was supported by the Australian Synchrotron Research Program, which is funded by the Commonwealth of Australia under the National Collaborative Research Infrastructure Strategy. The experimentalists especially thank the XOR beamline members and the APS user office for support. Use of the APS was supported by the U.S. Department of Energy under contract DE-AC02-06CH11357.

We acknowledge travel funding to the ESRF provided by the International Synchrotron Access Program (ISAP) managed by the Australian Synchrotron. The ISAP is funded by a National Collaborative Research Infrastructure Strategy grant provided by the Federal Government of Australia. We also appreciate and thank for the access and support of the ESRF management, User Office and beamline staff.

References

[1] K.-D. Liss, A. Bartels, A. Schreyer, H. Clemens, Texture Microstruct. 35 (3/4) (2003) 219–252.
[2] K. Yan, K.-D. Liss, U. Garbe, J. Daniels, O. Kirstein, H. Li, R. Dippenaar, Adv. Eng. Mater. 11/10 (2009) 771–773.
[3] K. Yan, D.G. Carr, M.D. Callaghan, K.-D. Liss, H. Li, Scr. Mater. 62 (2010) 246–249.
[4] K.-D. Liss, U. Garbe, H. Li, T. Schambron, J.D. Almer, K. Yan, Adv. Eng. Mater. 11/8 (2009) 637–640.
[5] K.-D. Liss, T. Schmoelzer, K. Yan, M. Reid, M. Peel, R. Dippenaar, H. Clemens, J. Appl. Phys. 106/11 (2009) 113526.
[6] J.E. Daniels, M. Drakopoulos, J. Synchrotron Radiat. 16 (2009) 463.
[7] Certified Scientific Software, Cambridge, MA, USA (2010).
[8] J. Böhm, A. Wanner, R. Kampmann, H. Franz, K.-D. Liss, A. Schreyer, H. Clemens, Nuclear Instrum. Method Phys. Res.: B (2003) 315–322.
[9] B. Jakobsen, H.F. Poulsen, U. Lienert, J. Almer, H.O. Sørensen, C. Gundlach, W. Pantleon, Science 312 (2006) 889–892.
[10] C.A. Bronkhorst, S.R. Kalidindi, L. Anand, Philos. Trans. R. Soc. A 341 (1992) 443.
[11] P. 11, R.Z. Landau, G. Shneck, A. Makov, Venkert, J. Mater. Sci. 42 (2007) 9775–9782.
[12] S.R. Agnew, M.H. Yoo, C.N. Tome, Acta Mater. 49 (2001) 4277–4289.
[13] M.R. Barnett, Mater. Sci. Eng. A 464 (2007) 8–16.
[14] K. Ahn, D. Yoo, M.H. Seo, S.-H. Park, K. Chung, Met. Mater. Int. 15 (4) (2009) 637–647.
[15] Y.-E. Kim, J.-W. Park, J. Cleveland, IAEA 2006; IAEA-TECDOC-1496.
[16] R.D. Shull, J.P. Cline, High Temp. Sci. 26 (1989) 95–117.
[17] L.A. Yeoh, K.-D. Liss, A. Bartels, H.F. Chladil, M. Avdeev, H. Clemens, R. Gerling, T. Buslaps, Scr. Mater. 57 (2007) 1145–1148.
[18] K.-D. Liss, R.E. Whitfield, W. Xu, T. Buslaps, L.A. Yeoh, X. Wu, D. Zhang, K. Xia, J. Synchrotron Radiat. 16 (2009) 825–834.
[19] I.J. Watson, K.-D. Liss, H. Clemens, W. Wallgram, T. Schmoelzer, T.C. Hansen, M. Reid, Adv. Eng. Mater. 11 (2009) 932–937.
[20] K. Thorogood. 'The Effect of Welding Thermal Cycles on the Microstructure and Texture of Zircaloy-4', Unpublished Bachelor of Engineering Thesis, School of Mechanical, Materials and Mechatronic Engineering. University of Wollongong, Wollongong, 2007.
[21] A.J.J. Van Ginneken, W.G. Burgers, Acta Crystallogr. 5 (1952) 548.
[22] M.-X. Zhang, P.M. Kelly, Acta Mater. 53 (2005) 1073–1084.
[23] K.-D. Liss, A. Bartels, H. Clemens, S. Bystrzanowski, A. Stark, T. Buslaps, F.-P. Schimansky, R. Gerling, C. Scheu, A. Schreyer, Acta Mater. 54 (14) (2006) 3721–3735.
[24] H. Clemens, W. Wallgram, S. Kremmer, V. Guther, A. Otto, A. Bartels, Adv. Eng. Mater. 10 (2008) 707.
[25] H. Clemens, H.F. Chladil, W. Wallgram, G.A. Zickler, R. Gerling, K.D. Liss, S. Kremmer, V. Guther, W. Smarslyg, Intermetallics 16 (2008) 827–833.
[26] M.J. Blackburn, in: R.I. Jaffee, N.E. Promisel (Eds.), The Science, Technology and Application of Titanium, Pergamon Press Ltd., Oxford, 1970, pp. 633–643.
[27] K.-D. Liss, A. Bartels, H. Clemens, T. Buslaps, D. Phelan, L.A. Yeoh, Adv. Eng. Mater. 10/4 (2008) 389–392.
[28] T. Schmoelzer, K.-D. Liss, M. Rester, K. Yan, A. Stark, W. Wallgram, M. Reid, M. Peel, R. Dippenaar, H. Clemens, Dynamic recovery and recrystallization of a multi-phase TiAl alloy during thermomechanical processing, Mater. Sci. Forum, in press.
[29] K.-D. Liss, T. d'Almeida, M. Kaiser, R. Hock, A. Magerl, J.F. Eloy, J. Appl. Phys. 106 (2009) 044914.
[30] K. Ichiyanagi, S.-I Adachi, S. Nozawa, Y. Hironaka, K.G. Nakamura, T. Sato, A. Tomita, S.-Y. Koshihara, Appl. Phys. Lett. 91 (2007) 231918.
[31] N.K. Bourne, G.T. Gray III, J.C.F. Millett, J. Appl. Phys. 106 (2009) 091301.